Electron Beam Energy Reconstruction for Neutrino Oscillation Measurements

M. Khachatryan,[1, *] A. Papadopoulou,[2, *] A. Ashkenazi,[2, †] F. Hauenstein,[1, 2]
A. Nambrath,[2] A. Hrnjic,[2] L.B. Weinstein,[1] O. Hen,[2] E. Piasetzky,[3] M. Betancourt,[4]
S. Dytman,[5] P. Coloma,[7] K. Mahn,[6] and and the CLAS and e4ν Collaborations

[1]*Old Dominion University, Norfolk, Virginia 23529*
[2]*Massachusetts Institute of Technology, Cambridge, Massachusetts 02139, USA*
[3]*School of Physics and Astronomy, Tel Aviv University, Tel Aviv 69978, Israel*
[4]*Fermi National Accelerator Laboratory, Batavia, IL*
[5]*University of Pittsburgh, Pittsburgh, PA*
[6]*Michigan State University, East Lansing, MI*
[7]*Instituto de Fisica Corpuscular, Universitat de Valencia and CSIC, Paterna, E-46980 Valencia, Spain
and Instituto de Fisica Teorica UAM/CSIC, Universidad Autonoma de Madrid, E-28049 Madrid, Spain*

Neutrinos exist in one of three types or "flavors" (ν_e, ν_μ or ν_τ) which oscillate from one to another when propagating through space. This phenomena is one of the few that cannot be described using the Standard Model of particle physics (see review in [1]). Thus, its experimental study can provide new insight into the nature of our universe (see review in [2]). Neutrinos oscillate as a function of their propagation distance divided by their energy (L/E). Therefore experiments extract oscillation parameters by measuring their energy distribution at different locations. As accelerator-based oscillation experiments cannot directly measure E, their interpretation relies heavily on phenomenological models of neutrino-nucleus interactions to infer E. Here we exploit the similarity of electron- and neutrino-nucleus interactions, and use electron scattering data with known beam energies to test energy reconstruction methods and interaction models. We find that even in simple interactions where no pions are detected, only a small fraction of events reconstruct to the correct incident energy. More importantly, widely-used interaction models reproduce the reconstructed energy distribution only qualitatively and the quality of the reproduction varies strongly with beam energy. This shows both the need and the pathway to improve current models to meet the requirements of next-generation, high-precision experiments such as Hyper-Kamiokande (HK, Japan) [3] and DUNE [4].

The three types of neutrinos are described in two different bases: flavor and mass. The weak nuclear interaction of neutrinos with other particles is described using flavor (ν_e, ν_μ, and ν_τ) while their propagation through space is described using mass. Each flavor state is a linear combination of the three mass states (ν_1, ν_2, and ν_3) [1].

In the simpler case of two neutrino flavors the oscillation probability from ν_μ to ν_e is given by [5]

$$P_{\nu_\mu \to \nu_e}(E, L) \approx \sin^2(2\theta) \sin^2\left(\frac{\Delta m^2 L}{4E}\right), \qquad (1)$$

where $\Delta m^2 = m_{\nu_1}^2 - m_{\nu_2}^2$ is the neutrino mass difference squared that determines the oscillation wavelength as a function of L/E, and θ is the neutrino mixing angle that determines the oscillation amplitude.

Accelerator-based measurements produce beams that predominantly contain either ν_μ or $\bar{\nu}_\mu$. At a distance L from the neutrino production point some ν_μ will oscillate to ν_e, resulting in fluxes of approximately

$$\Phi_e(E, L) \propto \qquad P_{\nu_\mu \to \nu_e}(E, L)\, \Phi_\mu(E, 0), \qquad (2)$$
$$\Phi_\mu(E, L) \propto \left[1 - P_{\nu_\mu \to \nu_e}(E, L)\right] \Phi_\mu(E, 0),$$

where the proportionality constant depends on the experiment geometry.

$\nu_\mu \to \nu_e$ oscillations are thus observed by measuring the neutrino fluxes $\Phi_e(E, L)$ and $\Phi_\mu(E, L)$ as a function of energy or distance. The three-flavor oscillation equations are similar but include additional terms. CP symmetry violation in the leptonic sector would add a phase (δ_{CP}) to the three-flavor oscillation with an opposite sign for neutrinos and anti-neutrinos ($\bar{\nu}$) [6, 7]. See Methods for details.

Experimentally, the neutrino flux is extracted from the measured neutrino interaction rate with atomic nuclei in neutrino detectors. This interaction rate is given by:

$$N_\alpha(E_{rec}, L) \propto \sum_i \int \Phi_\alpha(E, L)\sigma_i(E)f_{\sigma_i}(E, E_{rec})dE,$$
$$(3)$$

where $\sigma_i(E)$ is the neutrino interaction cross section for process i (e.g., quasi-elastic scattering, resonance production, etc.), α is the neutrino flavor, and E_{rec} is the neutrino energy reconstructed from the measured angles, momenta and/or energies of the detected particles.

$f_{\sigma_i}(E, E_{rec})$ is a smearing matrix relating the real (E) and reconstructed (E_{rec}) neutrino energies. E_{rec} differs from E due to both experimental effects (e.g., detector
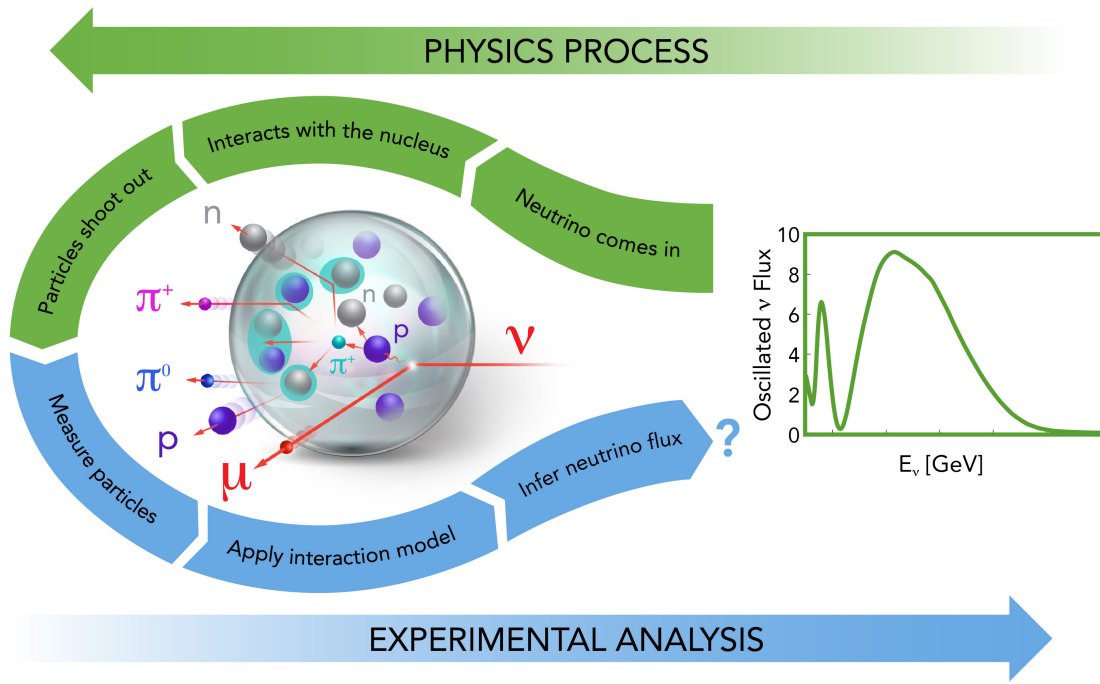
Fig. 1: **Neutrino oscillations and energy spectra measurements** | (Left) Neutrino energy spectra reconstruction depends on our ability to model the interaction of neutrinos with nuclei and the propagation of particles through the nucleus. This flow chart shows the process, starting with an oscillated far-detector incident-energy spectrum (green), differentiating the physical neutrino interactions (green arrows) from the experimental analysis (blue arrows), and ending up with an inferred incident-energy spectrum that hopefully matches the actual one.

resolutions, inefficiencies, backgrounds) and nuclear interaction effects (e.g., nucleon (proton or neutron) motion, meson currents, nucleon reinteraction). While experimental effects are generally understood, nuclear effects are irreducible and must be accounted for using theoretical models, typically implemented in neutrino event generators.

The precision to which oscillation parameters can be determined experimentally therefore depends on our ability to extract $\Phi_\alpha(E, L)$ from $N_\alpha(E_{rec}, L)$, see Fig. 1. This is largely determined by the accuracy of the theoretical models used to calculate $\sigma_i(E)$ and $f_{\sigma_i}(E, E_{rec})$. The models currently used have many free parameters that are poorly constrained and are "tuned" by each neutrino experiment. Current oscillation experiments report significant systematic uncertainties due to these interaction models [7–10] and simulations show that energy reconstruction errors can lead to significant biases in extracting δ_{CP} at DUNE [11]. There is a robust theoretical effort to improve these models [12–14].

Because there are no mono-energetic high-energy neutrino beams, these models cannot be tested for individual neutrino energies. Instead, experiments tune models of $\sigma_i(E)$ and $f_{\sigma_i}(E, E_{rec})$ to reproduce their near-detector data, where the unoscillated flux $\Phi(E, 0)$ is calculated from hadronic reaction rates [15–17].

While highly informative, such integrated constraints are insufficient to ensure that the models are correct for each value of E. Thus, for precision measurements using a broad-energy neutrino beam, the degree to which the near-detector data alone can constrain models is unclear, since the neutrino flux can be very different at the far detector due to oscillations.

Here we report the first measurement of $f_{\sigma_i}(E, E_{rec})$ for mono-energetic electron-nucleus scattering, and use it to test interaction models widely used by neutrino oscillation analyses. Both types of leptons, e and ν, interact similarly with nuclei. Both interact with nuclei via a vector current, while neutrinos have an additional axial-vector current. The nuclear ground state is the same in both cases and many of the nuclear reaction effects are similar. See Methods for details. Therefore, any model of neutrino interactions (vector+axial-vector) should also be able to reproduce electron (vector) interactions. The data presented here can therefore test neutrino-nucleus interaction models to be used in analysis of neutrino oscillation measurements. While previous work has compared these interaction models with inclusive electron scattering, (e, e'), [18, 19] this is the first comparison of semi-exclusive electron scattering data (data with one or more detected hadrons) with these interaction models.

We examined events with one detected electron, one

proton, and zero pions ($1p0\pi$), which were expected to be dominated by well-understood quasi-elastic (QE) scattering (i.e., by scattering of the lepton from a single moving nucleon in the nucleus). Even these simpler events reconstructed to the correct energy less than 50% of the time, and the models used dramatically overestimated the amount of mis-reconstructed events due to non-QE processes at the higher incident energies. This highlights a significant shortcoming in our current understanding of neutrino interactions which, if not corrected, could limit the exploitation of the full potential of next-generation, high-precision oscillation experiments, namely DUNE and HK.

I. ELECTRON DATA SELECTION

The experiment measured electron scattering from ^{4}He, ^{12}C, and ^{56}Fe nuclei at beam energies of 1.159, 2.257 and 4.453 GeV, detecting the scattered electron and knocked out particles over a wide range of angles and momenta in the CEBAF Large Acceptance Spectrometer (CLAS) [20] at the Thomas Jefferson National Accelerator Facility (Jefferson Lab). We detected electrons with energy $E_e \geq 0.4, 0.55$ and 1.1 GeV for $E_{beam} = 1.159, 2.257$ and 4.453 GeV respectively and angles $15° \leq \theta_e \leq 45°$, hadrons with momenta above 150 to 300 MeV/c and $10 - 20° \leq \theta_h \leq 140°$, and photons with energy $E_\gamma \geq 300$ MeV. These hadron detection thresholds are similar to those of neutrino detectors [21], however neutrino detectors have full angular coverage and lower lepton energy thresholds. See Methods for details concerning all aspects of this section.

The incident energies used here span the range of typical accelerator-based neutrino beams (Extended Data Fig. 1). The carbon data are relevant for scintillator-based experiments such as MINERνA and NOνA [22] and similar to the oxygen in water-based Čerenkov detectors such as Super-Kamiokande [7, 8] and Hyper-Kamiokande [23]. The iron is similar to the argon in the liquid argon time projection chambers of MicroBoone [24], the Fermilab short-baseline oscillation program [25] and DUNE [26].

We selected events with one electron and zero pions or photons from π^0 decay above threshold. We did this to maximize the contribution of well-understood events where the incident lepton scattered quasi-elastically from a single nucleon in the nucleus, as is done in many neutrino oscillation analyses [1, 27].

Electrons, unlike neutrinos, radiate bremsstrahlung photons in the electric field of the nucleus. We vetoed events where the photons from scattered-electron radiation were detected in CLAS.

We subtracted from our data contributions from events where unwanted pions or photons were produced but not detected due to the incomplete CLAS angular acceptance ($\approx 50\%$). We used events with a detected unwanted particle (e.g., pion or extra proton), and for each

event we constructed a "simulation" where we rotated the unwanted-particle momentum around the (known) momentum transfer direction many times to determine the probability P of detecting similar events. We then subtracted those events from our data set.

This produced an $(e, e')_{0\pi}$ data set where events included any number of detected or undetected protons and neutrons as well as charged pions and photons below the CLAS detection threshold. We also separately examined the subset of events with exactly one detected proton, i.e. $(e, e'p)_{1p0\pi}$, subtracting contributions from events with additional undetected protons above threshold.

We divided the yield by the integrated beam charge and target thickness to get a normalized yield. We corrected the data for the CLAS acceptance and for bremsstrahlung radiation to determine the cross section.

The electron-nucleon cross section is much more forward peaked than the neutrino cross section. We accounted for that by weighting each event by Q^4.

We considered several major sources of systematic uncertainties, including the angular dependence of the pion-production cross section (for the undetected-pion subtraction), the effects of fiducial cuts on undetected particle subtraction, photon identification cuts, the sector-to-sector variation of the cross section, and the CLAS acceptance corrections. The normalization uncertainty was about 3% and total point-to-point systematic uncertainties ranged from 7 to 25%, with the largest uncertainties for the smallest cross sections.

II. FROM NEUTRINO TO ELECTRON SCATTERING

We compared our mono-energetic electron data to predictions of the GENIE [28] simulation, which is used by most neutrino experiments in the USA and has an electron-scattering version (e-GENIE) that was recently overhauled to be consistent with the neutrino version [19]. GENIE includes quasi-elastic lepton scattering (QE), interactions of the lepton with two nucleons exchanging a meson (meson exchange currents or MEC, often referred to as "$2p2h$"), resonance production in nuclei (RES) and "deep inelastic scattering" (DIS, which also includes all non-resonant meson production), as well as rescattering (final state interactions) of the outgoing hadrons. We compared two GENIE "tunes", G2018 which reproduces measured neutrino [29] and electron inclusive cross sections, and SuSAv2 that uses modern, theoretically-inspired, recently-implemented QE and MEC models. See Methods for details.

We generated events using e-GENIE, propagated the events through CLAS fiducial cuts and acceptance maps to determine which particles were detected, and smeared the momenta of these particles based on the known CLAS resolution. We then analyzed the resulting simulated events using the same code as the data and compared
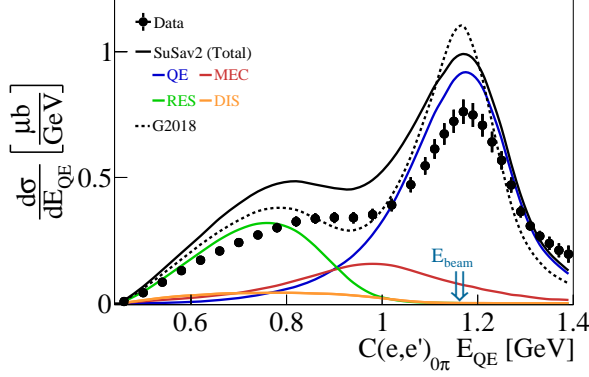
Fig. 2: **Quasi-Elastic Reconstructed Energy** | The 1.159 GeV $C(e,e')_{0\pi}$ cross section plotted as a function of the reconstructed energy E_{QE} for data (black points), GENIE SuSAv2 (solid black curve) and GENIE G2018 (dotted black curve). The colored lines show the contributions of different processes to the GENIE SuSAv2 cross section: QE (blue), MEC (red), RES (green) and DIS (orange). Error bars show the 68% (1σ) confidence limits for the statistical and point-to-point systematic uncertainties added in quadrature. Error bars are not shown when they are smaller than the size of the data point. Normalization uncertainty of 3% not shown.

the two. See Methods for details.

The inclusive electron-nucleus and neutrino-nucleus event distributions generated by e-GENIE (weighted by Q^4) and ν-GENIE are very similar [19]. This bolsters the relevance of our electron study to neutrino interactions.

III. INCIDENT ENERGY RECONSTRUCTION

There are two general approaches for reconstructing the incident neutrino energy, based on the particle detection capabilities of the neutrino detector.

Water Čerenkov detectors only measure charged leptons and pions. If the neutrino scattered quasi-elastically (QE) from a stationary nucleon in the nucleus, its energy can be reconstructed from the measured lepton as:

$$E_{QE} = \frac{2M_N\epsilon + 2M_N E_l - m_l^2}{2(M_N - E_l + k_l\cos\theta_l)}, \qquad (4)$$

where $\epsilon \approx 20$ MeV is the average nucleon separation energy, M_N is the nucleon mass, and $(m_l, E_l, k_l, \theta_l)$ are the scattered lepton mass, energy, momentum, and angle.

Figure 2 shows the E_{QE} distribution for 1.159 GeV $C(e,e')_{0\pi}$ events, which are most relevant for T2K and HK. We observe a broad peak centered at the real beam energy with a large tail extending to lower energies. The peak is doppler-broadened by the motion of the nucleons

in the nucleus. The tail is caused by non-quasi-elastic reactions that pass the $(e,e')_{0\pi}$ selection. The tail is cut off at the lowest energies by the CLAS minimum detected electron energy of 0.4 GeV.

The SuSAv2 e-GENIE peak has the correct width, but is somewhat larger than the data. It overestimates the tail by about 25%. The G2018 e-GENIE peak also exceeds the data, but is too narrow, with a Gaussian width of $\sigma = 76$ MeV, compared to 89 MeV for the data. This is due to inexact modeling of the nuclear ground state momentum distribution. The tail dips below the data at around 0.9 GeV, and is larger than the data at lower reconstructed energies. Neither model describes the data quantitatively well.

Tracking detectors measure all charged particles above their detection thresholds. The "calorimetric" incident neutrino energy is then the sum of all the detected particle energies:

$$E_{cal} = \sum E_i + \epsilon, \qquad (5)$$

where E_i are the detected nucleon kinetic energies and the lepton and meson total energies and ϵ is the average total removal energy for the detected particles.

Figure 3 shows the cross section as a function of E_{cal} for 1.159, 2.257 and 4.453 GeV $C(e,e'p)_{1p0\pi}$ events and 2.257 and 4.453 GeV $Fe(e,e'p)_{1p0\pi}$ events. All spectra show a sharp peak at the real beam energy, followed by a large tail at lower energies. For carbon, only 30–40% of the events reconstruct to within 5% of the real beam energy, see Extended Data Table 1. For iron this fraction is only 20–25%, highlighting the crucial need to well model the low-energy tail of these distributions. e-GENIE overpredicts the fraction of events in the peak at 1.159 GeV and significantly underpredicts it at 4.453 GeV, see Extended Data Fig. 2a.

e-GENIE using SuSAv2 dramatically overpredicts the peak cross section at 1.159 and 2.257 GeV, and significantly underestimates the peak cross section at 4.453 GeV, see Extended Data Fig. 2b. e-GENIE using the older G2018 models overestimates the peak cross section at all three incident energies. It also reconstructs the peak position (i.e. the incident energy) to be 10, 25 and 36 MeV too low for ^{4}He, C and Fe, respectively, at all three beam energies. This is due to an error in the G2018 QE models.

This beam-energy dependence of the data-GENIE discrepancy could have significant implications for neutrino flux reconstruction.

At 1.159 GeV, e-GENIE using SuSAv2 slightly overpredicts the low energy tail and e-GENIE using G2018 is reasonably close. Both models dramatically overpredict the low energy tail at the higher beam energies (see Fig. 3 insets). The tail seems to be dominated by resonance production (plus DIS at 4.453 GeV) that did not result in the production of other charged particles above detection threshold. This overprediction is also seen in inclusive electron scattering from the proton and deuteron,
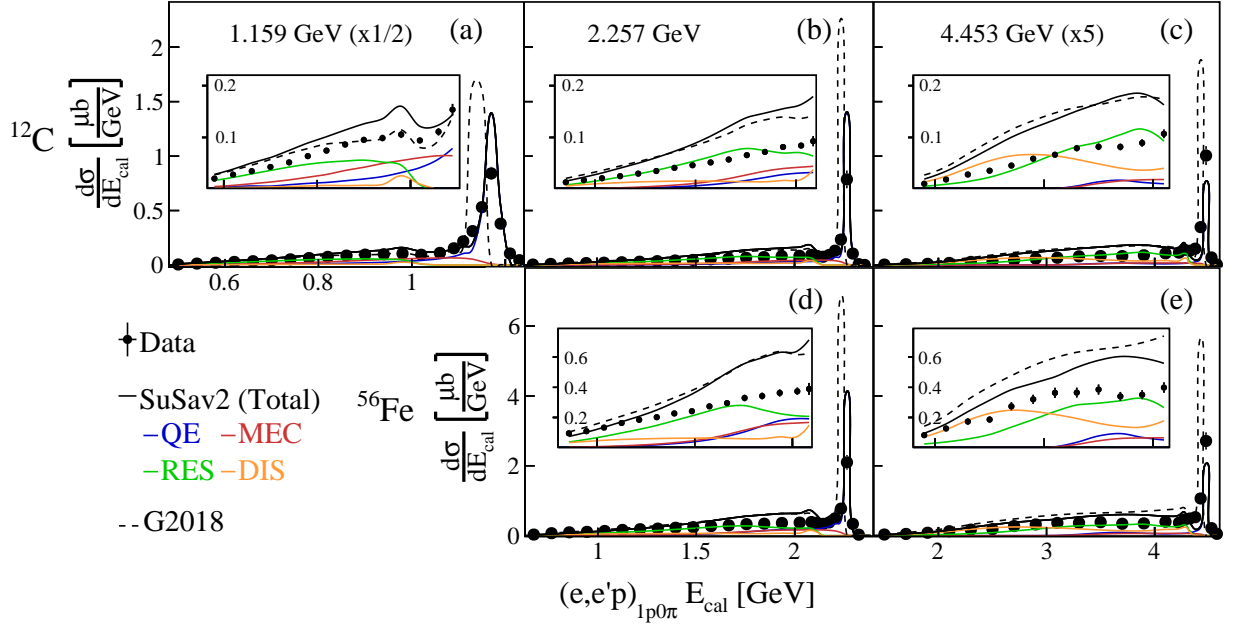
Fig. 3: **Calorimetric Reconstructed Energy** | The $A(e, e'p)_{1p0\pi}$ cross section plotted as a function of the reconstructed calorimetric energy E_{cal} for data (black points), SuSAv2 (black solid curve) and G2018 (black dotted curve). Different panels show results for different beam energy and target nucleus combinations: (top row) Carbon target at (left to right) 1.159, 2.257 and 4.453 GeV, and (bottom) Iron target at (left) 2.257 and (right) 4.453 GeV incident beam. The 1.159 GeV yields have been scaled by $1/2$ and the 4.453 GeV yields have been scaled by 5 to have the same vertical scale. The insets show the cross sections with the same horizontal scale and an expanded vertical scale. Line colors, error bars, and uncertainties are the same as in Fig. 2.

and thus appears to be due to the electron-nucleon interaction, rather than to the nuclear modeling [19]. See Methods for details.

SuSAv2 describes the peak cross section equally well for C and for Fe, while G2018 over estimates the peak cross section more for Fe than for C. Both models predict a greater peak fraction (relative to the data) for Fe than for C, particularly at 2.2 GeV. See Extended Data Fig. 2 and Extended Data Table 1.

While the $(e, e')_{0\pi}$ quasi-elastic reconstruction of Eq. 4 gives a much broader peak at the true beam energy than the calorimetric energy E_{cal} due to the effects of nucleon motion (see Extended Data Fig. 4), it has the same tail of lower energy events for the same $(e, e'p)_{1p0\pi}$ data set.

IV.   TRANSVERSE VARIABLES AND MODEL TUNING

Neutrino experiments use "single transverse variables" to enhance their sensitivity to different aspects of the reaction mechanism. These STVs are independent of the incident neutrino energy [30–32],

$$\vec{P_T} = \vec{P}_T^{e'} + \vec{P}_T^p \tag{6}$$

$$\delta\alpha_T = \arccos \frac{\vec{P}_T^{e'} \cdot \vec{P_T}}{P_T^{e'} P_T} \tag{7}$$

$$\delta\phi_T = \arccos \frac{\vec{P}_T^{e'} \cdot \vec{P}_T^p}{P_T^{e'} P_T^p} \tag{8}$$

where $\vec{P}_T^{e'}$ and $\vec{P}_T^p$ are the three-momenta of the detected lepton and proton perpendicular to the direction of the incident lepton, respectively. Purely quasi-elastic events without final state interactions will have small P_T, consistent with the motion of the struck nucleon. Events with small P_T should thus reconstruct to the correct incident energy. $\delta\alpha_T$ measures the angle between $\vec{P_T}$ and the transverse momentum transfer ($\vec{q}_T = -\vec{P}_T^{e'}$) in the transverse plane and is isotropic in the absence of final state interactions. $\delta\phi_T$ measures the opening angle between the detected proton momentum and the transverse momentum transfer and is forward peaked. $\delta\phi_T$ is intended to probe regions where MEC/$2p2h$ events dominate [30–32].

The P_T distribution for 2.257 GeV C$(e, e'p)_{1p0\pi}$ is shown in Fig. 4 (and the other targets and energies are shown in Extended Data Fig. 5). Both data and e-
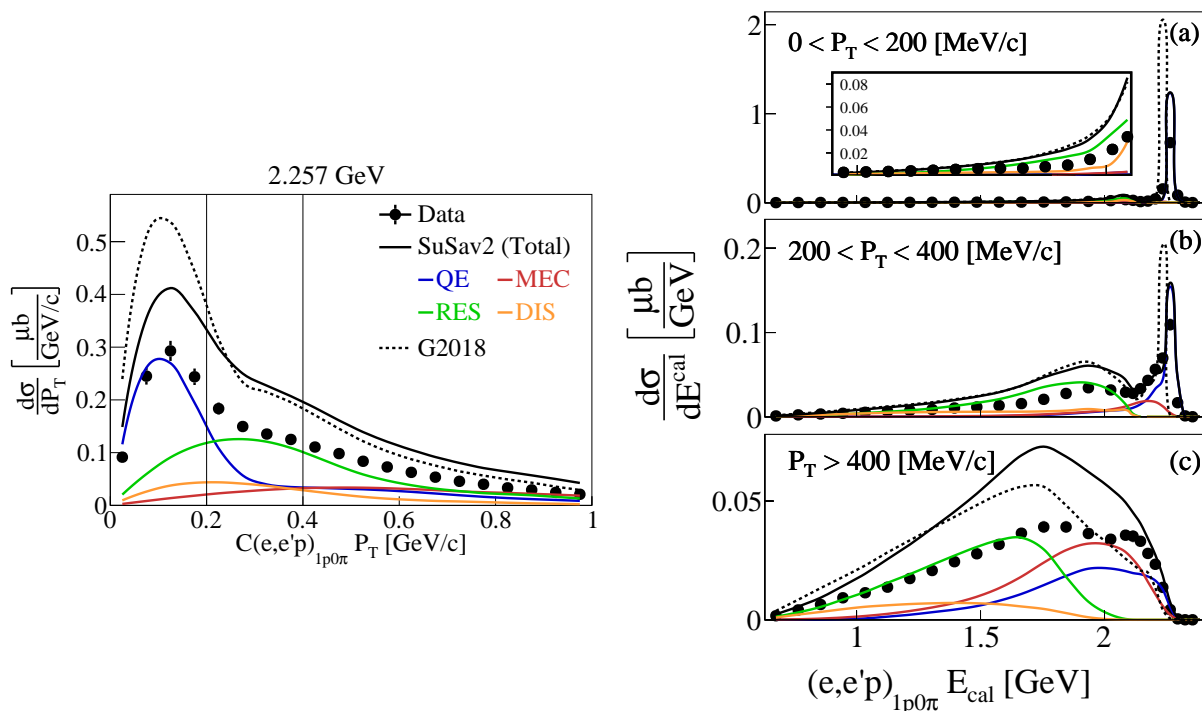
Fig. 4: **Reconstructed energies and perpendicular momenta** | (Left) the 2.257 GeV $C(e, e'p)_{1p0\pi}$ cross section plotted P_T for data (black points), SuSav2 (black solid line) and G2018 (black dashed line). The vertical lines at 200 MeV/c and at 400 MeV/c separate the three bins in P_T. (Right) The cross section plotted versus E_{cal} for: (top) $P_T < 200$ MeV/c, (middle) 200 MeV/$c \leq P_T \leq 400$ MeV/c, and (bottom) $P_T > 400$ MeV/c. Line colors, error bars, and uncertainties are the same as in Fig. 2.

GENIE peak at relatively low momenta, as expected, and both have a large tail extending out to 1 GeV/c and containing about half of the measured events. The high-P_T tail is predominantly due to resonance production that did not result in an additional pion or nucleon above the detection threshold. e-GENIE using SuSAv2 reproduces the shape of the data moderately well, suggesting adequate reaction modeling, including the contribution of non-QE processes such as resonance production.

As expected, both data and e-GENIE/SuSAv2 events with $P_T < 200$ MeV/c almost all reconstruct to the correct incident energy. However, events with $P_T \geq 400$ MeV/c do not reconstruct to the correct energy and are poorly reproduced by e-GENIE.

This disagreement indicates that including high-P_T data in oscillation analyses could bias the extracted parameters. As high-P_T data accounts for $25-50\%$ of the measured events, care must be taken to improve the models implemented in GENIE, so that they can reproduce the high-P_T data. This will be especially true at the higher incident neutrino energies expected for DUNE.

The $\delta\alpha_T$ distributions become progressively less isotropic at higher energies and heavier targets, indicating the increasing importance of FSI and of non-QE reaction mechanisms. GENIE agrees best with data at the lowest beam energy. At the higher beam energies

GENIE describes the relatively flat smaller angles much better than the back-angle peak. GENIE also describes the lowest energy $\delta\phi_T$ distribution. At higher energies, GENIE overestimates the height of the forward peak. See Extended Data Fig. 6.

V. SUMMARY

In conclusion, we have used Jefferson Lab CLAS electron-nucleus scattering data with known incident energies to perform the first test of our ability to reconstruct incident neutrino energies from measured lepton-nucleus collisions. This is a crucial step in the neutrino-oscillation experiment analysis chain.

Most of the $1p0\pi$ events do not reconstruct to the correct incident energy. The interaction model describes the size but not the exact shape of the low-energy tail for quasi-elastic energy reconstruction at 1.159 GeV, despite reproducing differential inclusive electron-scattering cross sections. The same interaction model dramatically over-estimates the low-energy tail for calorimetric energy reconstruction at 2.257 and 4.453 GeV electrons. The more modern SuSAv2 model describes the quasielastic events better than the older G2018 model, but there are still significant discrepancies.

As we enter a precision era of neutrino studies, it is critical to improve the neutrino-models to the same level of accuracy and precision. Electron scattering offers a way to test aspects of these models that complements theoretical calculations and neutrino near-detector data.

Combining the neutrino energy reconstruction studies presented here with the standard near-detector neutrino data analyses could significantly reduce the systematic modeling uncertainties of next generation oscillation experiments. This could be complemented by efforts such as DUNE-PRISM which would provide quasi-monochromatic neutrino beams by making linear combinations of off-axis neutrino fluxes. DUNE-PRISM would be sensitive to axial currents and would have very different systematic uncertainties than electron measurements. Future experiments with the improved CLAS12 spectrometer (see Methods for details) will extend the electron measurements to more nuclei, much smaller scattering angles, and to a wider range of momentum transfers. All of these will be needed to reduce the systematic modeling uncertainties of next generation oscillation experiments.

[1] M. Tanabashi *et al.* (Particle Data Group), Phys. Rev. D **98**, 030001 (2018).
[2] R. Mohapatra *et al.*, Rept. Prog. Phys. **70**, 1757 (2007).
[3] K. Abe *et al.* (Hyper-Kamiokande), (2018), arXiv:1805.04163 [physics.ins-det].
[4] B. Abi *et al.* (DUNE), (2018), arXiv:1807.10334 [physics.ins-det].
[5] M. Gonzalez-Garcia and Y. Nir, Rev. Mod. Phys. **75**, 345 (2003).
[6] M. Fukugita and T. Yanagida, Phys. Lett. B **174**, 45 (1986).
[7] K. Abe *et al.* (T2K), Nature **580**, 339 (2020).
[8] K. Abe *et al.* (T2K), Phys. Rev. Lett. **121**, 171802 (2018).
[9] L. Alvarez-Ruso *et al.*, Prog. Part. Nucl. Phys. **100**, 1 (2018).
[10] M. Acero *et al.* (NOvA), Phys. Rev. D **98**, 032012 (2018).
[11] A. M. Ankowski, P. Coloma, P. Huber, C. Mariani, and E. Vagnoni, Phys. Rev. D **92**, 091301 (2015).
[12] N. Rocco, Frontiers in Physics **8**, 116 (2020).
[13] S. Dolan, G. D. Megias, and S. Bolognesi, Phys. Rev. D **101**, 033003 (2020).
[14] N. Rocco, A. Lovato, and O. Benhar, Phys. Rev. Lett. **116**, 192501 (2016).
[15] L. Aliaga *et al.* (MINERνA Collaboration), Phys. Rev. D **94**, 092005 (2016).
[16] K. K. Maan (NOvA), PoS **ICHEP2016**, 931 (2016).
[17] L. Haegel (T2K), in *18th International Workshop on Neutrino Factories and Future Neutrino Facilities Search* (2017) arXiv:1701.02559 [hep-ex].
[18] A. M. Ankowski and A. Friedland, Phys. Rev. D **102**, 053001 (2020), arXiv:2006.11944 [hep-ph].
[19] A. Papadopolou *et al.*, Phys. Rev. D **103**, 113003 (2021), arXiv:2009.07228 [nucl-th].
[20] B. A. Mecking *et al.*, Nucl. Instrum. Meth. **A503**, 513 (2003).
[21] M. Betancourt *et al.* (MINERvA), Phys. Rev. Lett. **119**, 082001 (2017).
[22] L. Aliaga *et al.*, Nucl. Instrum. Methods **A743**, 130 (2014).
[23] K. Abe *et al.* (Hyper-Kamiokande), (2018), arXiv:1805.04163 [physics.ins-det].
[24] R. Acciarri *et al.* (MicroBooNE), JINST **12**, P02017 (2017).
[25] M. Antonello *et al.* (MicroBooNE, LAr1-ND, ICARUS-WA104), (2015), arXiv:1503.01520 [physics.ins-det].
[26] R. Acciarri *et al.* (DUNE), (2015), arXiv:1512.06148 [physics.ins-det].
[27] T. Katori and M. Martini, J. Phys. G **45**, 013001 (2018).
[28] C. Andreopoulos *et al.*, Nucl. Inst. and Meth. A **614**, 87 (2010).
[29] P. Abratenko *et al.* (MicroBooNE), Phys. Rev. Lett. **123**, 131801 (2019).
[30] X.-G. Lu, L. Pickering, S. Dolan, G. Barr, D. Coplowe, Y. Uchida, D. Wark, M. O. Wascko, A. Weber, and T. Yuan, Phys. Rev. C **94**, 015503 (2016).
[31] K. Abe *et al.* (The T2K Collaboration), Phys. Rev. D **98**, 032003 (2018).
[32] X.-G. Lu *et al.* (MINERvA Collaboration), Phys. Rev. Lett. **121**, 022504 (2018).
[33] M. Freund, Phys. Rev. D **64**, 053003 (2001).
[34] A. Cervera, A. Donini, M. Gavela, J. G. Cádenas], P. Hernández, O. Mena, and S. Rigolin, Nuclear Physics B **579**, 17 (2000).
[35] A. Cervera, A. Donini, M. Gavela, J. G. Cádenas, P. Hernández, O. Mena, and S. Rigolin, Nuclear Physics B **593**, 731 (2001).
[36] M. Osipenko *et al.* (CLAS), Nucl. Phys. A **845**, 1 (2010), arXiv:1002.3776 [nucl-ex].
[37] K. S. Egiyan *et al.* (CLAS), Phys. Rev. Lett. **96**, 082501 (2006), arXiv:nucl-ex/0508026.
[38] D. Protopopescu *et al.* (CLAS), Nucl. Phys. A **748**, 357 (2005), arXiv:nucl-ex/0405021.
[39] A. V. Stavinsky *et al.* (CLAS), Phys. Rev. Lett. **93**, 192301 (2004), arXiv:hep-ex/0405064.
[40] R. A. Niyazov *et al.* (CLAS), Phys. Rev. Lett. **92**, 052303 (2004), [Erratum: Phys.Rev.Lett. 92, 099903 (2004)], arXiv:nucl-ex/0308013.
[41] K. S. Egiyan *et al.* (CLAS), Phys. Rev. C **68**, 014313 (2003), arXiv:nucl-ex/0301008.
[42] O. Hen *et al.*, Science **346**, 614 (2014).
[43] R. M. Sealock *et al.*, Phys. Rev. Lett. **62**, 1350 (1989).
[44] L. W. Mo and Y.-S. Tsai, Rev. Mod. Phys. **41**, 205 (1969).
[45] A. De Pace, M. Nardi, W. Alberico, T. Donnelly, and A. Molinari, Nucl. Phys. A **726**, 303 (2003).
[46] T. Katori, "Meson exchange current (mec) models in neutrino interaction generators," (2013), arXiv:1304.6014 [nucl-th].
[47] J. Tena-Vidal *et al.* (GENIE), (2021), arXiv:2104.09179 [hep-ph].
[48] C. Berger and L. Sehgal, Phys. Rev. D **76**, 113004 (2007).
[49] R. P. Feynman, M. Kislinger, and F. Ravndal, Phys. Rev. D **3**, 2706 (1971).
[50] A. Bodek and U. K. Yang, J. Phys. G **29**, 1899 (2003).

[51] T. Yang, C. Andreopoulos, H. Gallagher, K. Hofmann, and P. Kehayias, The European Physical Journal C **63**, 1 (2009), 0904.4043.

[52] T. Sjöstrand, S. Mrenna, and P. Skands, Journal of High Energy Physics **2006**, 026 (2006), hep-ph/0603175.

[53] C. Andreopoulos, C. Barry, S. Dytman, H. Gallagher, T. Golan, R. Hatcher, G. Perdue, and J. Yarba, (2015), arXiv:1510.05494 [hep-ph].

[54] S. Dytman and A. Meyer, AIP Conference Proceedings **1405**, 213 (2011).

[55] R. Merenyi, W. A. Mann, T. Kafka, W. Leeson, B. Saitta, J. Schneps, M. Derrick, and B. Musgrave, Phys. Rev. D **45**, 743 (1992).

[56] S. G. Mashnik, A. J. Sierk, K. K. Gudima, and M. I. Baznat, J. Phys. Conf. Ser. **41**, 340 (2006).

[57] K. Abe *et al.* (The T2K Collaboration), Phys. Rev. D **101**, 012007 (2020).

[58] N. Markov *et al.* (The CLAS Collaboration), Phys. Rev. C **101**, 015208 (2020).

[59] M. Osipenko, *A Kinematically Complete Measurement of the Proton Structure Function F_2 in the Resonance Region and Evaluation of its Moments*, Ph.D. thesis, Moscow State University (2002).

[60] K. Abe *et al.* (T2K), "Improved constraints on neutrino mixing from the t2k experiment with 3.13×10^{21} protons on target," (2021), arXiv:2101.03779 [hep-ex].

[61] B. Abi *et al.* (DUNE), Eur. Phys. J. C **80**, 978 (2020), arXiv:2006.16043 [hep-ex].

Author Contributions The CEBAF Large Acceptance Spectrometer was designed and constructed by the CLAS Collaboration and Jefferson Lab. Data acquisition, processing and calibration, Monte Carlo simulations of the detector and data analyses were performed by a large number of CLAS Collaboration members, who also discussed and approved the scientific results. The analysis presented here was performed by M.K., A.P., and A.A. with guidance from A.A., F.H., O.H., E.P., and L.B.W., and was reviewed by the CLAS Collaboration. S.D., M.B., and K.M. provided expertise on neutrino scattering. S.D. helped guide development of *e*-GENIE. P.C. performed a simulation of the DUNE sensitivity to the oscillation parameters, and determined the impact of our results on the fit.

Author Information Reprint and permission information is available at www.nature.com/reprints. The authors declare no competing financial interests. Readers are welcome to comment on the online version of the paper. Publisher's note: Springer Nature remains neutral with regard to jurisdictional claims in published maps and institutional affiliations. Correspondence and requests for materials should be addressed to O.H. (hen@mit.edu).

Full Author List M. Khachatryan,[1] A. Papadopoulou,[2] A. Ashkenazi,[2] F. Hauenstein,[1,2] A. Nambrath,[2] A. Hrnjic,[2] L.B. Weinstein,[1] O. Hen,[2] E. Piasetzky,[3] M. Betancourt,[4] S. Dytman,[5] P. Coloma,[7] K. Mahn,[6] S. Adhikari,[18] M.J. Amaryan,[1] Giovanni Angelini,[20] H. Atac,[43] L. Barion,[22] M. Battaglieri,[44,24] I. Bedlinskiy,[34] A. Beck,[2] F. Benmokhtar,[15] A. Bianconi,[46,27] A.S. Biselli,[16,10] F. Bossù,[11] S. Boiarinov,[44] W.J. Briscoe,[20] W.K. Brooks,[45,44] D. Bulumulla,[1] V.D. Burkert,[44] D.S. Carman,[44] J.C. Carvajal,[18] A. Celentano,[24] P. Chatagnon,[28] V. Chesnokov,[41] T. Chetry,[33] G. Ciullo,[22,17] L. Clark,[47] B.A. Clary,[13] E.O. Cohen,[3] P.L. Cole,[32,21] M. Contalbrigo,[22] V. Crede,[19] R. Cruz-Torres,[2] A. D'Angelo,[25,40] N. Dashyan,[51] R. De Vita,[24] M. Defurne,[11] A. Denniston,[2] A. Deur,[44] S. Diehl,[13] C. Djalali,[37,42] M. Duer,[3] R. Dupre,[28] H. Egiyan,[44] M. Ehrhart,[8] A. El Alaoui,[45] L. El Fassi,[33] L. Elouadrhiri,[44] P. Eugenio,[19] R. Fersch,[12] A. Filippi,[26] T.A. Forest,[21] G. Gavalian,[44,35] G.P. Gilfoyle,[39] K.L. Giovanetti,[30] F.X. Girod,[44] D.I. Glazier,[47] E. Golovatch,[41] R.W. Gothe,[42] K.A. Griffioen,[50] M. Guidal,[28] L. Guo,[18,44] H. Hakobyan,[45,51] M. Hattawy,[1] T.B. Hayward,[50] D. Heddle,[12,44] K. Hicks,[37] A. Hobart,[28] M. Holtrop,[35] Y. Ilieva,[42,20] D.G. Ireland,[47] B.S. Ishkhanov,[41] E.L. Isupov,[41] H.S. Jo,[31] K. Joo,[13] D. Keller,[49] A. Khanal,[18] M. Khandaker,[36,] C.W. Kim,[20] W. Kim,[31] I. Korover,[2] V. Kubarovsky,[44,38] S.E. Kuhn,[1] L. Lanza,[25] M. Leali,[46,27] P. Lenisa,[22,17] K. Livingston,[47] I .J .D. MacGregor,[47] D. Marchand,[28] N. Markov,[44] L. Marsicano,[24] V. Mascagna,[46] B. McKinnon,[47] S. May-Tal Beck,[2] T. Mineeva,[45] M. Mirazita,[23] V. Mokeev,[44,41] A Movsisyan,[22] C. Munoz Camacho,[28] P. Nadel-Turonski,[44] K. Neupane,[42] S. Niccolai,[28] G. Niculescu,[30] M. Osipenko,[24] A.I. Ostrovidov,[19] M. Paolone,[43] L.L. Pappalardo,[22,17] R. Paremuzyan,[35] K. Park,[31,] E. Pasyuk,[44] O. Pogorelko,[34] J. Poudel,[1] Y. Prok,[1,49] D. Protopopescu,[47] J. Pybus,[2] M. Ripani,[24] B. Raue,[18] J. Ritman,[29] A. Rizzo,[25,40] G. Rosner,[47] P. Rossi,[44,23] F. Sabatié,[11] C. Salgado,[36] A. Schmidt,[20]

R.A. Schumacher,[10] E.P. Segarra,[2] Y.G. Sharabian,[44] U. Shrestha,[37] Iu. Skorodumina,[42,41] D. Sokhan,[47] O. Soto,[23] N. Sparveris,[43] S. Stepanyan,[44,1] I.I. Strakovsky,[20] S. Strauch,[42,20] N. Tyler,[42] R. Tyson,[47] M. Ungaro,[44,38] L. Venturelli,[46,27] H. Voskanyan,[51] E. Voutier,[28] D. Watts,[48] X. Wei,[44] M.H. Wood,[9,42] N. Zachariou,[48] J. Zhang,[49] and Z.W. Zhao,[14]

[1] Old Dominion University, Norfolk, Virginia 23529. [2] Massachusetts Institute of Technology, Cambridge, Massachusetts 02139, USA. [3] School of Physics and Astronomy, Tel Aviv University, Tel Aviv 69978, Israel. [4] Fermi National Accelerator Laboratory, Batavia, IL. [5] University of Pittsburgh, Pittsburgh, PA. [6] Michigan State University, East Lansing, MI. [7] Instituto de Fisica Corpuscular, Universitat de Valencia and CSIC, Paterna, E-46980 Valencia, Spain and Instituto de Fisica Teorica UAM/CSIC, Universidad Autonoma de Madrid, E-28049 Madrid, Spain. [8] Argonne National Laboratory, Argonne, Illinois 60439. [9] Canisius College, Buffalo, NY. [10] Carnegie Mellon University, Pittsburgh, Pennsylvania 15213. [11] IRFU, CEA, Université Paris-Saclay, F-91191 Gif-sur-Yvette, France. [12] Christopher Newport University, Newport News, Virginia 23606. [13] University of Connecticut, Storrs, Connecticut 06269. [14] Duke University, Durham, North Carolina 27708-0305. [15] Duquesne University, 600 Forbes Avenue, Pittsburgh, PA 15282. [16] Fairfield University, Fairfield CT 06824. [17] Universita' di Ferrara , 44121 Ferrara, Italy. [18] Florida International University, Miami, Florida 33199. [19] Florida State University, Tallahassee, Florida 32306. [20] The George Washington University, Washington, DC 20052. [21] Idaho State University, Pocatello, Idaho 83209. [22] INFN, Sezione di Ferrara, 44100 Ferrara, Italy. [23] INFN, Laboratori Nazionali di Frascati, 00044 Frascati, Italy. [24] INFN, Sezione di Genova, 16146 Genova, Italy. [25] INFN, Sezione di Roma Tor Vergata, 00133 Rome, Italy. [26] INFN, Sezione di Torino, 10125 Torino, Italy. [27] INFN, Sezione di Pavia, 27100 Pavia, Italy. [28] Universit'e Paris-Saclay, CNRS/IN2P3, IJCLab, 91405 Orsay, France. [29] Institute fur Kernphysik (Juelich), Juelich, Germany. [30] James Madison University, Harrisonburg, Virginia 22807. [31] Kyungpook National University, Daegu 41566, Republic of Korea. [32] Lamar University, 4400 MLK Blvd, PO Box 10009, Beaumont, Texas 77710 [33] Mississippi .State University, Mississippi State, MS 39762-5167. [34] National Research Centre Kurchatov Institute - ITEP, Moscow, 117259, Russia. [35] University of New Hampshire, Durham, New Hampshire 03824-3568. [36] Norfolk State University, Norfolk, Virginia 23504. [37] Ohio University, Athens, Ohio 45701. [38] Rensselaer Polytechnic Institute, Troy, New York 12180-3590. [39] University of Richmond, Richmond, Virginia 23173. [40] Universita' di Roma Tor Vergata, 00133 Rome Italy. [41] Skobeltsyn Institute of Nuclear Physics, Lomonosov Moscow State University, 119234 Moscow, Russia. [42] University of South Carolina, Columbia, South Carolina 29208. [43] Temple University, Philadelphia, PA 19122. [44] Thomas Jefferson National Accelerator Facility, Newport News, Virginia 23606. [45] Universidad Técnica Federico Santa María, Casilla 110-V Valparaíso, Chile. [46] Università degli Studi di Brescia, 25123 Brescia, Italy. [47] University of Glasgow, Glasgow G12 8QQ, United Kingdom. [48] University of York, York YO10 5DD, United Kingdom. [49] University of Virginia, Charlottesville, Virginia 22901. [50] College of William and Mary, Williamsburg, Virginia 23187-8795. [51] Yerevan Physics Institute, 375036 Yerevan, Armenia.

Methods

Three-flavor neutrino oscillation.

Eq. 1 gives the neutrino oscillation probability for the simplified case of only two types of neutrino. The full three-flavor probability for $\nu_\mu \to \nu_e$ oscillation (in vacuum) is given by [33–35]

$$P_{\nu_\mu \to \nu_e}(E, L) \approx A \sin^2 \frac{\Delta m_{13}^2 L}{4E} \tag{9}$$
$$-B \cos \left(\frac{\Delta m_{13}^2 L}{4E} + \delta_{CP} \right) \sin \frac{\Delta m_{13}^2 L}{4E},$$

where $\Delta m_{13}^2 = m_{\nu_1}^2 - m_{\nu_3}^2$ is the neutrino mass difference squared that determines the oscillation wavelength as a function of L/E and δ_{CP} is a phase that might break charge-parity (CP) symmetry. The coefficients A and B depend primarily on the neutrino oscillation mixing angles, $A = \sin^2 \theta_{23} \sin^2 2\theta_{13}$ and $B = -\frac{\sin 2\theta_{12} \sin 2\theta_{23}}{2 \sin \theta_{13}} \sin \frac{\Delta m_{21}^2 L}{4E} \sin^2 2\theta_{13}$. The different flavor neutrinos (labelled ν_e, ν_μ and ν_τ) are linear combinations of the different mass neutrinos labelled $1, 2, 3$.

Lepton cross sections

Neutrinos and electrons interact with atomic nuclei by exchanging intermediate vector bosons, a massive $W^\pm$ or Z for the neutrino and a massless photon for the electron. Electrons interact via a vector current ($j_{EM}^\mu = \bar{u}\gamma^\mu u$) and neutrinos interact via vector and axial-vector ($j_{CC}^\mu = \bar{u}\gamma^\mu(1 - \gamma^5)u \frac{-ig_W}{2\sqrt{2}}$) currents.

Fundamental considerations (the number of independent momenta, Lorentz invariance, parity conservation, and current conservation) give an inclusive (e, e') electron-nucleon elastic scattering cross section that depends on only two structure functions:

$$\frac{d^2\sigma^e}{dx dQ^2} = \frac{4\pi\alpha^2}{Q^4} \left[\frac{1-y}{x} F_2^e(x, Q^2) + y^2 F_1^e(x, Q^2) \right] \tag{10}$$

Here F_1^e and F_2^e are the standard electromagnetic vector structure functions, $Q^2 = \mathbf{q}^2 - \nu^2$ is the squared momentum transfer and $\mathbf{q}$ and ν are the three-momentum and energy transfers, $x = Q^2/(2m\nu)$ is the Bjorken scaling variable, m is the nucleon mass, $y = \nu/E_e$ is the electron fractional energy loss, and α is the fine structure constant. This formula shows the simplest case where $Q^2 \gg m^2$.

The corresponding inclusive charged current (CC) $(\nu, l^\pm)$ neutrino-nucleon elastic cross section (where $l^\pm$ is the outgoing charged lepton) has a similar form. The vector part of the current is subject to the same fundamental considerations as above, but the axial-vector part of the current does not conserve parity. This leads to a third, axial, structure function:

$$\frac{d^2\sigma^\nu}{dx dQ^2} = \frac{G_F^2}{2\pi} \left[\frac{1-y}{x} F_2^\nu(x, Q^2) + y^2 F_1^\nu(x, Q^2) \right.$$
$$\left. -y(1 - y/2) F_3^\nu(x, Q^2) \right]. \tag{11}$$

Here F_1^ν and F_2^ν are the parity-conserving neutrino-nucleus (vector) structure functions, F_3^ν is the axial structure function, and G_F is the Fermi constant. The vector form factors (F_1^ν and F_2^ν) have both vector-vector and axial-axial contributions.

The strength of the interaction is very different: $4\pi\alpha^2/Q^4$ for electrons versus $G_F^2/(2\pi)$ for neutrinos, where the factor of $1/Q^4$ in the electron cross section is due to the photon propagator. When compensated for the factor of $1/Q^4$, the shapes of the electron- and neutrino-nucleus cross sections, as calculated in GENIE, are very similar [19].

Nuclear medium effects such as nucleon motion, binding energy, two-body currents, and final state interactions will be similar or identical.

In order to calculate the electron-nucleus cross section in GENIE, we changed the interaction strength, set the axial structure functions to zero, and set the axial-axial parts of the vector structure functions to zero.

Thus, models of the neutrino-nucleus cross section must be able to describe the more limited electron-nucleus cross section.

Experimental setup and particle identification: CLAS used a toroidal magnetic field with six sectors of drift chambers, scintillation counters, Čerenkov counters and electromagnetic calorimeters to identify electrons, pions, protons, and photons, and to reconstruct their trajectories [20]. The six sectors functioned as six independent spectrometers. See Extended Data Fig. 9a.

We used the e2a data, which was measured in 1999 and was used in many published analyses [36–41]. We measured the momentum and charge of the outgoing charged particles from their measured positions in the drift chambers and the curvature of their trajectories in the magnetic field. We identified electrons by requiring that the track originated in the target, produced a time-correlated signal in the Čerenkov counter, and deposited enough energy in the electromagnetic calorimeter. We identified charged pions and protons by requiring that the track originated in the target and that the measured time of flight agreed (to within ±three times the standard deviation of the detector resolution) with that calculated from the particle's momentum and assumed mass. We identified photons by requiring a signal in the electromagnetic calorimeter which implied a velocity greater than about $0.96c$ (see Ref. [42] for details).

We corrected low-momentum protons for energy losses traversing the target and detector material. We used the CLAS GEANT Monte Carlo Simulation to simulate the proton energy loss in CLAS as a function of proton momentum. The maximum correction was about 20 MeV/c for a proton momentum of 300 MeV/c. The correction was negligible for protons with momenta greater than 600 MeV/c.

We detected protons with momenta $p_p \geq 300$ MeV/c and angles $\theta_p \geq 10°$, charged pions with momenta $p_\pi \geq 150$ MeV/c and angles $\theta_{\pi^+} \geq 10°$ and $\theta_{\pi^-} \geq 22°$,

and photons with energy $E_\gamma \geq 300$ MeV and $8 \leq \theta_\gamma \leq 45°$. We applied separate fiducial cuts for electrons, π^-, positive particles, and photons, to select momentum-dependent regions of CLAS where the detection efficiency was constant and close to one. We also determined the minimum electron angle (as a function of electron momentum p) for each beam energy as

$$\theta_e^{1.1} \geq 17° + \frac{7°}{p\,[\text{GeV}]} \tag{12}$$

$$\theta_e^{2.2} \geq 16° + \frac{10.5°}{p\,[\text{GeV}]} \tag{13}$$

$$\theta_e^{4.4} \geq 13.5° + \frac{15°}{p\,[\text{GeV}]} \tag{14}$$

and the minimum π^- angle as

$$\theta_{\pi^-}^{1.1} \geq 17° + \frac{4°}{p\,[\text{GeV}]}$$

and

$$\theta_{\pi^-}^{2.2,4.4} \geq 25° + \frac{7°}{p\,[\text{GeV}]}$$

for $p_{\pi^-} < 0.35$ GeV/c and

$$\theta_{\pi^-}^{2.2,4.4} \geq 16° + \frac{10°}{p\,[\text{GeV}]}$$

for $p_{\pi^-} \geq 0.35$ GeV/c. The minimum π^+ and proton angle was $\theta > 12°$ for all data sets and momenta.

We measured the delivered beam charge using the CLAS Faraday Cup.

Energy Calibration: The beam energy equaled the injector energy plus the pass number times the linac energy. The three-pass beam energy was measured using the Hall A arc measurement and the four pass energy was measured using the Hall C arc measurement. These gave a central linac energy of 1.0979 GeV and Hall B one-, two-, and four-pass beam energies of $1.159, 2.257$, and 4.453 GeV, respectively. We assigned an uncertainty of 2×10^{-3} to these energies, based on the difference between the Hall A and Hall C measurements.

We used elastic electron scattering from hydrogen to correct the electron momentum as a function of angle for uncertainties in the CLAS magnetic field and in CLAS tracking chamber locations. These corrections also significantly narrowed the elastic peak width. Typical correction factors were less than 1%. We checked the momentum correction factors at lower scattered electron energies using the $H(e, e'\pi+)X$ and $^3\text{He}(e, e'pp)X$ reactions and found that they gave the correct missing mass for the undetected neutron (see Extended Data Fig. 9).

Nucleon removal energies: The average nucleon removal energy, ϵ, used in reconstructing the incident energies in Eqs. 4 and 5, was determined from the data. We used $\epsilon = M_A - M_{A-1} - m_p + \Delta\epsilon$, where $M_A - M_{A-1} - m_p$ is the difference in the binding energies for knocking a proton out of nucleus A. We adjusted $\Delta\epsilon$ so that the peaks in the E_{cal} spectrum for low-P_T events reconstructed to the correct beam energy. We found $\Delta\epsilon = 5$ and 11 MeV for ^{12}C and ^{56}Fe, respectively, which are consistent with average excitation energies from single-nucleon knockout from nuclei.

Subtraction of undetected pions and photons: Because the CLAS geometrical coverage is incomplete, we needed to subtract for undetected pions and photons to achieve a true 0π event sample. We assumed that the photons came from either radiation by the outgoing electron approximately parallel to its motion or from π^0 decay. We identified the radiated photons by requiring that they be detected within $\delta\phi \leq 30°$ and $\delta\theta \leq 40°$ of the scattered electron and removed them from the data set.

We determined the undetected pion or photon contribution from the events with detected pions or photons. We assumed that the pion-production cross section was independent of $\phi_{q\pi}$, the angle between the electron-scattering plane (the plane containing the incident and scattered electrons and the virtual photon) and the hadron plane (the plane containing the virtual photon and pion). For each detected $(e, e'\pi)$ event, we rotated the pion around the momentum transfer direction $\vec{q}$ randomly many times. For each rotation we determined if the particle would have been detected, i.e., if the particle was within the fiducial region of the detector. If it was, we used acceptance maps to determine the probability that it would have been detected. The particle acceptance is then $A_\pi = N_{det}/N_{rot}$, where N_{rot} is the number of rotations and N_{det} is the number of times the pion would have been detected. Then the corresponding number of undetected $(e, e'\pi)$ events for that detected $(e, e'\pi)$ event is $(N_{rot} - N_{det})/N_{det}$. We used that as a weight to subtract for the undetected pion events.

For example, if one specific $(e, e'\pi)$ event would have been detected 250 times out of 1000 rotations, then we inferred that for each event we detected, there were three more that we did not detect. We calculated the reconstructed energy (and other appropriate variables) for that event and subtracted it from the reconstructed energy spectrum (and other corresponding distributions) with a weight of three. We did this separately for π^+, π^- and photons.

In order to subtract the undetected $(e, e'p\pi)$ and $(e, e'p\gamma)$ events to get the $(e, e'p)_{0\pi}$ sample, we rotated the proton and pion (or photon) together around $\vec{q}$ and determined the number of detected proton-only events N_{det}^p and the number of detected proton and pion events $N_{det}^{p\pi}$. We used $(N_{det}^p - N_{det}^{p\pi})/N_{det}^{p\pi}$ as a weight to subtract for the undetected $(e, e'p\pi)$ and $(e, e'p\gamma)$ events. We also subtracted the $(e, e'p)$ event sample for extra protons in the same way to get a true $1p0\pi$ sample. The proton and pion multiplicity plots are shown in Extended Data Fig. 3. e-GENIE dramatically overpredicts the number

of events with large proton and pion multiplicities.

We also accounted for the effects of, for example, events with two detected pions (or photons). When we rotated these events, each rotated event could have been detected as a 2π event, a 1π event, or a 0π event. If it appeared as a 0π event, we subtracted its contribution from the various 0π spectra as described above. If it appeared as a 1π event, we included it in the set of 1π events with the appropriate negative weight. We then treated it as a regular 1π event, which we then rotated and added to the 0π data set as described above. (This is where it gets complicated. Some of the detected 1π events are actually 2π events with an undetected pion. When we account for the effects of these events, we are left with fewer true 1π events. This reduces the contamination of the 1π events in the 0π channel.)

In practice, we started with the highest multiplicity events, e.g. $(e, e'3\pi)$, and subtracted their contributions to each of the detected lower multiplicity channels, e.g., $(e, e'2\pi)$, $(e, e'\pi)$, and $(e, e'0\pi)$. We then worked recursively, rotating higher multiplicity events to determine and subtract their contributions to the lower multiplicity channels, and then considering each of the lower multiplicity channels in turn.

We considered event multiplicities up to three pions and photons (total) for (e, e') and up to three protons, pions and photons (total) for $(e, e'p)$, where the subtraction converged. The effects of the subtraction (and its convergence) can be seen in Extended Data Fig. 7. The number of events with an undetected $\pi^{\pm}$ or photon is about equal to the number of events with a detected $\pi^{\pm}$ or photon, consistent with the $\approx 50\%$ CLAS geometrical acceptance. The effect of including two $\pi^{\pm}$ or photon events is much less than that of the one $\pi^{\pm}$ or photon events and the effect of including three $\pi^{\pm}$ or photon events is negligible.

We tested the subtraction method by applying it to GENIE-simulated data. The resulting subtracted spectra agreed reasonably with the true $1p0\pi$ spectra.

Cross Section Determination: We determined the inclusive $1.159\ 37.5°$ GeV $C(e, e')$ cross section (see Fig. Extended Data Fig. 3b):

$$\frac{d\sigma}{d\Omega d\omega} = \frac{N_e}{\Delta\Omega N_i N_t}$$

where N_e is the number of detected electrons in Sector 1 within $36° \leq \theta_e \leq 39°$ and a $12°$ range in ϕ_e, $\Delta\Omega = \sin\theta_e d\theta_e d\phi_e = 6.68$ msr, N_i is the number of incident electrons, and $N_t = 0.179$ g/cm^2 $= 8.95 \times 10^{-9}$ nuclei/μbarn. The measured cross sections are in reasonable agreement with the GENIE predictions and are also consistent with the SLAC measurements at lower and higher energies [43].

We determined the cross section as a function of reconstructed energy (for particles above the minimum angles (see Eq. 14)) in several steps. We first weighted all events by a factor of Q^4 to account for the major difference in electron- and neutrino-nucleus scattering.

1. Determine the number of weighted $(e, e')_{0\pi}$ or $(e, e'p)_{1p0\pi}$ events, corrected for events with undetected pions, photons and (if appropriate) extra protons, as a function of reconstructed energy,

2. divide the number of events by the number of target nuclei per area and the number of incident beam electrons to get the normalized yield,

3. correct for electron radiation by multiplying the resulting spectra by the ratio of e-GENIE without electron radiation divided by e-GENIE with electron radiation (see Fig. Extended Data Fig. 8g-i). This includes a mutiplicative factor to account for the effects of internal radiation,

4. correct for electron and proton acceptance and other detector effects using e-GENIE. The acceptance correction factor is the ratio of the number of true $(e, e'p)_{1p0\pi}$ events without detector effects to the number of true $(e, e'p)_{1p0\pi}$ events with detector effects. The detector effects included momentum resolution, fiducial (acceptance) cuts, and efficiency maps. The fiducial cuts determine the useful areas of the detector as a function of particle momenta and angles, and the efficiency maps describe the efficiency of the detector as a function of particle momenta and angles. This factor corrects the effective electron and proton solid angles to almost 4π. It excludes all electrons, pions and protons below their minimum angles (see Eq. 14), and

5. divide by the reconstructed energy bin width.

We calculated the acceptance correction factor using both G2018 and SuSav2. We used the bin-by-bin average of the two as the acceptance correction factor and the bin-by-bin difference divided by $\sqrt{12}$ as the uncertainty. See Fig. Extended Data Fig. 8a-f.

GENIE Simulations: We generated events with the electron-scattering version of GENIE (e-GENIE), one of the standard neutrino event generators. e-GENIE has been significantly modified recently to fix known issues, to use reaction mechanisms as close to those of ν-GENIE as possible (version v3.00.06), and to include the effects of the real photon part of electron bremsstrahlung [44]. We used CLAS acceptance maps to determine the probability that each particle was detected and smeared the momenta of the particles with an effective CLAS resolution (we used electrons and proton momentum resolutions of 0.5% and 1%, respectively, for the 2.257 and 4.453 GeV data and 1.5% and 3% for the 1.159 GeV data which was taken with a lower torus magnetic field). We then analyzed the events in the same way as the data.

We used e-GENIE with the newly implemented SuSAv2 models for electron-nucleon quasielastic scattering (QE) and for MEC. The SuSAv2 QE model is based

on the superscaling exhibited by inclusive electron scattering data and uses Relativistic Mean Field theory to describe both the nuclear initial state and the cross section modifications due to the outgoing nucleon reinteracting with the residual nucleus [13]. The SuSAv2 MEC model describes the lepton interaction with a transverse electromagnetic isovector meson-change current (which excites two-particle two-hole ($2p2h$) states) in the framework of [45]. Because it uses superscaling to describe a wide range of nuclei with a single scaling function, SuSAv2 was never intended to model nuclei lighter than ^{12}C.

We compared that with the older e-GENIE version (tune G18_10a_02_11a, referred to here as G2018) which used the Local Fermi Gas model; the Rosenbluth cross section for electron-nucleon quasi-elastic scattering and the empirical Dytman model [46] of MEC (Meson Exchange currents or $2p2h$ currents), which describes it as a Gaussian distribution located between the quasi-elastic and Δ peaks [47].

Both the SuSAv2 and G2018 tunes used the Berger-Sehgal model [48] of electron-nucleon resonance production (RES), which includes cross sections of 16 resonances calculated in the Feynman-Kislinger-Ravndal (FKR) model [49], without interference between them. There are slight differences in the tuning parameters for the two tunes.

Deep inelastic scattering (DIS) is modeled using Bodek and Yang [50]. Hadronization is modeled using an approach which transitions gradually between the AGKY model [51] and the PYTHIA 6 model [52]. At low values of the hadronic invariant mass W, the Bodek-Yang differential cross section is scaled by tunable parameters that depend on the multiplicity of hadrons in the final-state [53].

e-GENIE used two models of the final state interactions of outgoing protons and pions with the residual nucleus. G2018 used the Intranuke package [54, 55] with hA2018, an empirical data-driven method, using the cross section of pions and nucleons with nuclei as a function of energy up to 1.2 GeV, and the CEM03 [56] calculation normalized to low-energy data for higher energies. SuSAv2 used hN, a full intra-nuclear cascade calculation of the interactions of pions, kaons, photons, and nucleons with nuclei. In the hN model, each outgoing particle can interact successively with any or all the nucleons it encounters on its path leaving the nucleus, and any particles created in those interactions can also subsequently reinteract. The ability of the two models to describe hadron-nucleus data is very similar.

e-GENIE includes radiative corrections based on the formalism of Ref. [44] to account for radiation of a real photon by the electron either before after scattering, for radiation and reabsorption of a virtual photon (vertex correction), and for virtual pair production by the exchanged photon (vacuum polarization). This includes radiated real photons up to 15% of the incident electron energy. The vertex correction and vacuum polarization corrections were on the order of 6%.

While many of the reaction mechanisms in GENIE have been tuned to approximately reproduce inclusive electron scattering cross sections, the hadron-production part of the models have rarely, if ever, been compared to precision data.

This version of e-GENIE [19] and ν-GENIE [29] described inclusive electron- and charged current neutrino-scattering cross sections moderately well. The SuSAv2 models described the data around the QE peak and in the dip region between the QE peak and the first resonance peak significantly better than the G2018 tune. The data was less well described at energy transfers at and above the first resonance peak (the region where RES and DIS scattering dominate).

The difference between data and GENIE at smaller reconstructed energies attributed to the RES and DIS processes (described in Section III) might be due to either (a) the GENIE RES and DIS processes were tuned to ν-deuteron data only and thus the axial+vector response is better constrained than the vector part, or (b) the distinction between RES and DIS is artificial and some resonance contributions might be double counted in the two processes. There is a suggestion that GENIE also overpredicts resonance production in neutrino-nucleus interactions (see Figs. 13-16 in Ref. [57]), lending support to the second hypothesis.

Systematic Uncertainties We considered several major sources of systematic uncertainties, including the angular dependence of the pion-production cross section (for the undetected-pion subtraction), the effects of fiducial cuts on undetected particle subtraction, photon identification cuts, the sector-to-sector variation of the data to e-GENIE ratio, the model-dependence of the acceptance correction, and uncertainties in the normalization measurement.

When we rotated events containing pions around the momentum transfer vector, we assumed that the cross section did not depend on $\phi_{q\pi}$. We tested the $\phi_{q\pi}$ independence of the pion-production cross section by weighting the subtraction using the measured $\phi_{q\pi}$-dependent $H(e, e'p\pi)$ cross sections of Ref. [58]. This changed the subtracted spectra by about 1% and was included as a systematic uncertainty.

The subtraction of events with undetected pions depends on the CLAS acceptance for such particles. The final spectrum should be independent of the CLAS pion acceptance. We estimated the effect of varying the CLAS acceptance on the undetected particle subtraction by comparing the results using the nominal fiducial cuts and using fiducial cuts with the ϕ acceptance in each CLAS sector reduced by 6° or about 10–20%. This changed the resulting subtracted spectra by about 1% at 1.159 and 2.257 GeV and by 4% at 4.453 GeV. This difference was included as a point-to-point systematic uncertainty.

We also varied the photon identification cuts. We identified photons as neutral particle hits in the calorimeter with a velocity greater than two standard deviations (3σ

at 1.159 GeV) below the mean of the photon velocity peak (at $v = c$). We varied this limit by $\pm 0.25\sigma$. This gave an uncertainty in the resulting subtracted spectra of 0.1%, 0.5% and 2% at 1.159, 2.257 and 4.453 GeV, respectively.

CLAS has six almost-identical sectors (see Extended Data Fig. 9a). The primary difference among the sectors is the distribution of dead detector channels. We attempted to account for these dead channels in our fiducial cuts (where we cut away dead or partially dead regions of the detector) and in our acceptance maps, where we measured the effect of the dead detectors on the particle detection efficiency and applied that efficiency to the particles generated in the e-GENIE monte carlo simulation. If our fiducial cuts and acceptance maps completely accounted for the effect of the dead and inefficient detector channels, then the ratio of data to e-GENIE should be the same for all six sectors.

We discarded sectors with anomalous data to e-GENIE ratios and used the variance of the ratios for the remaining sectors as a measure of the uncertainty in the measured normalized yields. This gave a point-to-point systematic uncertainty of 6%.

We calculated the acceptance correction factors using both G2018 and SuSav2. We shifted the G2018 results so that the energy reconstruction peaks lined up at the correct beam energy. We used the bin-by-bin average of the two correction factors as the acceptance correction factor and the bin-by-bin difference divided by $\sqrt{12}$ as the uncertainty. We averaged the uncertainty over the entire peak to avoid large uncertainties due to small misalignments. See Extended Data Fig. 8a-f.

The overall normalization was determined using inclusive 4.4 GeV H(e, e') measurements. The measured and simulated H(e, e') cross sections agreed to within an uncertainty of 3%, which we use as a normalization uncertainty [59].

We added the statistical uncertainty and the point-to-point systematic uncertainties in quadrature and displayed them on the data points.

Future CLAS12 Experiments Jefferson Lab Experiment E12-17-006, "Electrons for Neutrinos: Addressing Critical Neutrino-Nucleus Issues" (scientific rating: A) will take more data on more targets with a greater kinematical range using the upgraded CLAS12 detector. The approved experiment includes measurements on ^{4}He, C, Ar and Sn with 1, 2, and 4 GeV electron beams, as well as measurements on O with 1 and 2 GeV electron beams. The 1 and 2 GeV measurements will be performed with a minimum electron scattering angle of $5°$, compared to a minimum CLAS angle of about $20°$. This will extend the measurements down to the much lower momentum transfers typical of some neutrino experiments. It will therefore allow comparison with the lower beam-energy data of T2K and HyperK. The first part of the experiment is scheduled to run in the second half of 2021.
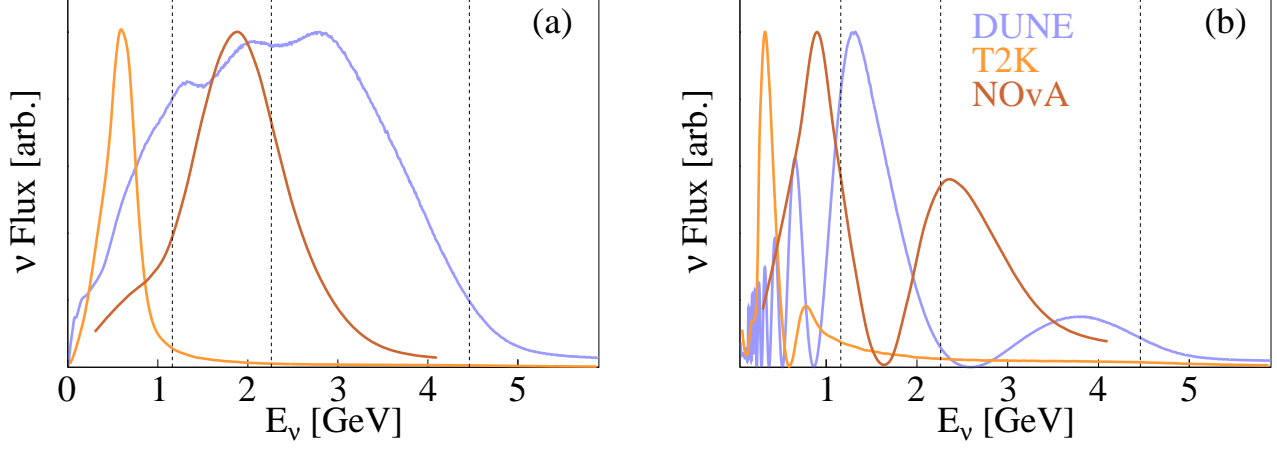
Extended Data

Fig. Extended Data Fig. 1: The expected energy distribution of different ν_μ beams, (left) before oscillation at the near detector and (right) after oscillation at the far detector [60, 61]. The vertical lines show the three electron beam energies of this measurement. The NOνA far-detector beam flux is calculated using the near detector flux and the neutrino oscillation parameters from the Particle Data Group.

Table Extended Data Table 1: $(e, e'p)_{1p0\pi}$ events reconstructed to the correct beam energy. Peak Fraction refers to the fraction of events reconstructed to the correct beam energy and Peak Sum refers to the integrated weighted cross section (as shown in Fig. 3) reconstructed to the correct beam energy. The peak integration windows are $1.1 \leq E_{cal} \leq 1.22$ GeV, $2.19 \leq E_{cal} \leq 2.34$ GeV, and $4.35 \leq E_{cal} \leq 4.60$ GeV, respectively, for the three incident beam energies. Uncertainties are shown graphically in Extended Data Fig. 2. SuSAv2 is not intended to model nuclei lighter than ^{12}C.

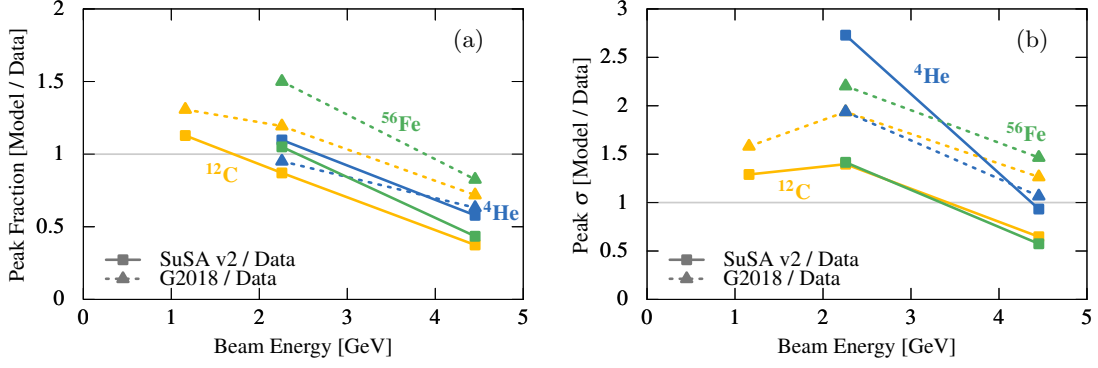| | | 1.159 GeV | | 2.257 GeV | | 4.453 GeV | |
		Peak Fraction	Peak Sum [μb]	Peak Fraction	Peak Sum [μb]	Peak Fraction	Peak Sum [μb]
^{4}He	Data	-	-	41	0.48	38	0.15
	SuSAv2	-	-	45	1.31	22	0.14
	G2018	-	-	39	0.93	24	0.16
^{12}C	Data	39	4.13	31	1.26	32	0.34
	SuSAv2	44	5.33	27	1.76	12	0.20
	G2018	51	6.53	37	2.44	23	0.43
^{56}Fe	Data	-	-	20	3.73	23	1.01
	SuSAv2	-	-	21	5.28	10	0.58
	G2018	-	-	30	8.22	19	1.48

Fig. Extended Data Fig. 2: (left) The ratio of e-GENIE to data for the fraction of the weighted cross section that reconstructs to the correct incident energy, plotted vs incident energy and, (right) the e-GENIE-data weighted cross section ratio for events that reconstruct to the correct incident energy, plotted vs incident energy. The triangles and dashed lines indicate the G2018/data ratios and the squares and solid lines indicate the SuSAv2/data ratios. SuSAv2 is not intended to model nuclei lighter than ^{12}C. Yellow shows the carbon, blue shows helium, and green shows iron. Error bars show the 68% (1σ) confidence limits for the statistical and point-to-point systematic uncertainties added in quadrature. Error bars are not shown when they are smaller than the size of the data point. Normalization uncertainties of 3% not shown.
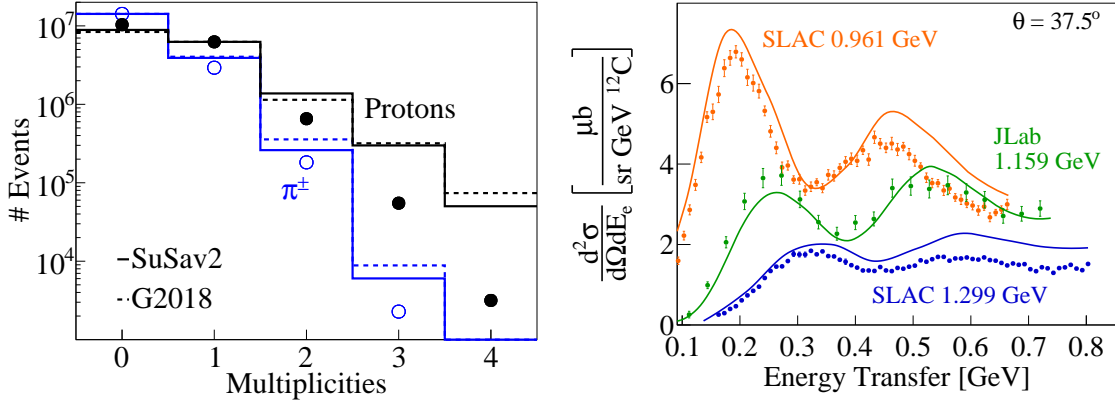

Fig. Extended Data Fig. 3: (Left) The proton (black) and charged pion (blue) multiplicities for data (points), SuSav2 (solid histogram) and G2018 (dashed histogram) for 2.257 GeV carbon. (Right) Comparison between the inclusive C(e, e') cross sections measured at 37.5° for data (points) and SuSav2 (lines) for the 0.961 and 1.299 GeV SLAC data [43] and our 1.159 GeV CLAS data. Error bars show the 68% (1σ) confidence limits for the statistical and point-to-point systematic uncertainties added in quadrature. Error bars are not shown when they are smaller than the size of the data point. Normalization uncertainties of 3% not shown.
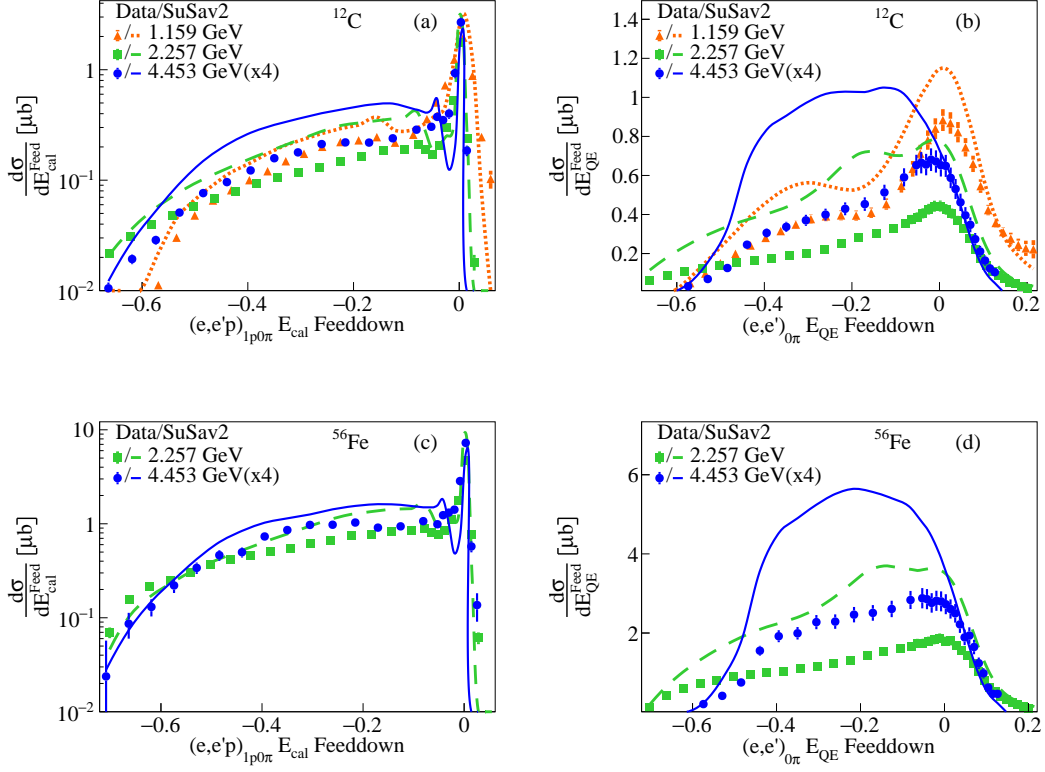
Fig. Extended Data Fig. 4: Energy feed-down cross–sections $(E_{rec} - E_{true})/E_{true}$ for data (points) and SuSav2 (lines) for 1.159 GeV (red triangles and dotted lines), 2.257 GeV (green squares and dashed lines) and 4.453 GeV (blue dots and solid lines) for (a) C E^{cal}, (b) C E^{QE}, (c) Fe E^{cal}, and (d) Fe E^{QE}. The plots are area normalized and each bin has been scaled by the bin width. Error bars show the 68% (1σ) confidence limits for the statistical and point-to-point systematic uncertainties added in quadrature. Error bars are not shown when they are smaller than the size of the data point. Normalization uncertainties of 3% not shown.
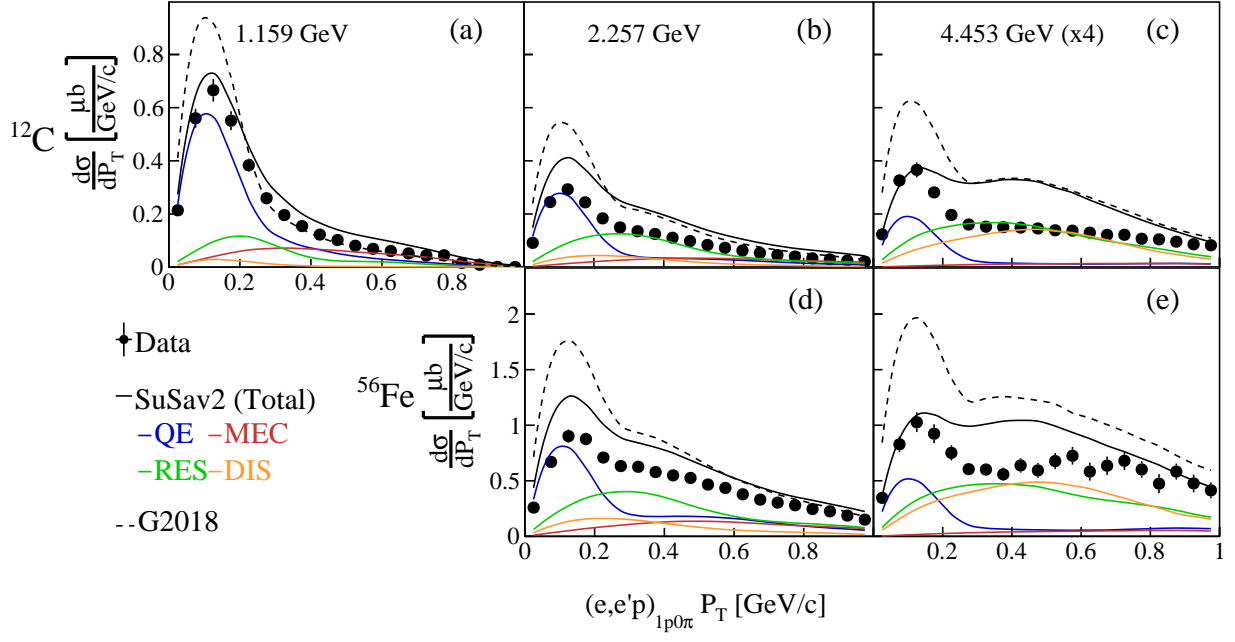
Fig. Extended Data Fig. 5: The cross section plotted vs transverse missing momentum P_T for data (black points), SuSAv2 (black solid curve) and G2018 (black dotted curve). Different panels show results for different beam energy and target nucleus combinations: (top row) Carbon target at (left to right) 1.159, 2.257 and 4.453 GeV, and (bottom) Iron target at (left) 2.257 and (right) 4.453 GeV. The 4.453 GeV yields have been scaled by four to have the same vertical scale. Colored lines show the contributions of different processes to the SuSAv2 GENIE simulation: QE (blue), MEC (red), RES (green) and DIS (orange). Error bars show the 68% (1σ) confidence limits for the statistical and point-to-point systematic uncertainties added in quadrature. Error bars are not shown when they are smaller than the size of the data point. Normalization uncertainties of 3% not shown.
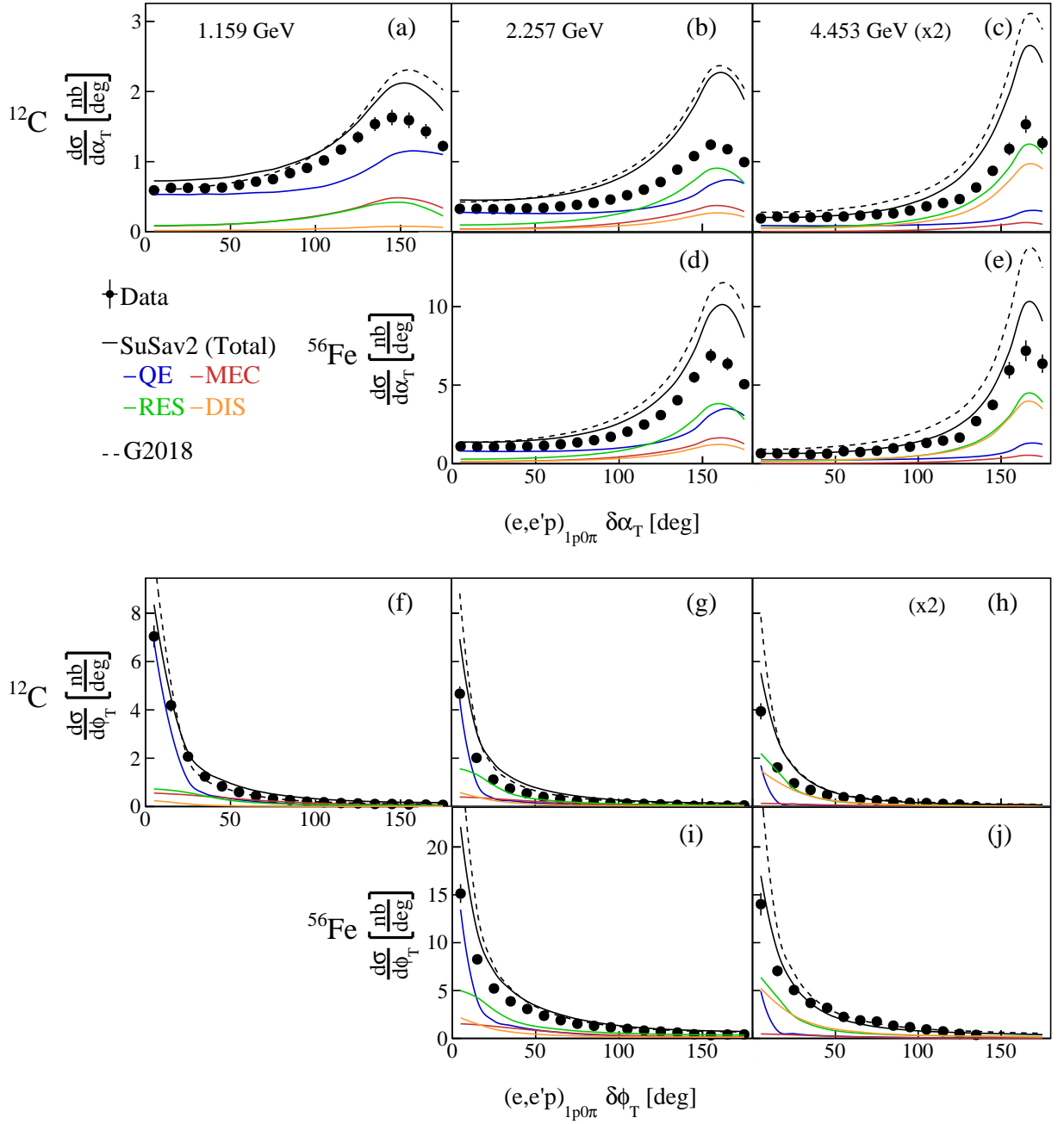
Fig. Extended Data Fig. 6: The cross section plotted vs $\delta\alpha_T$ (a-e) and vs $\delta\phi_T$ (f-j) for data (black points), SuSAv2 (black solid curve) and G2018 (black dotted curve). Different panels show results for different beam energy and target nucleus combinations: (top row) Carbon target at (left to right) 1.159, 2.257 and 4.453 GeV, and (bottom) Iron target at (left) 2.257 and (right) 4.453 GeV. The 4.453 GeV yields have been scaled by two to have the same vertical scale. Colored lines show the contributions of different processes to the SuSAv2 GENIE simulation: QE (blue), MEC (red), RES (green) and DIS (orange). Error bars show the 68% (1σ) confidence limits for the statistical and point-to-point systematic uncertainties added in quadrature. Error bars are not shown when they are smaller than the size of the data point. Normalization uncertainties of 3% not shown.
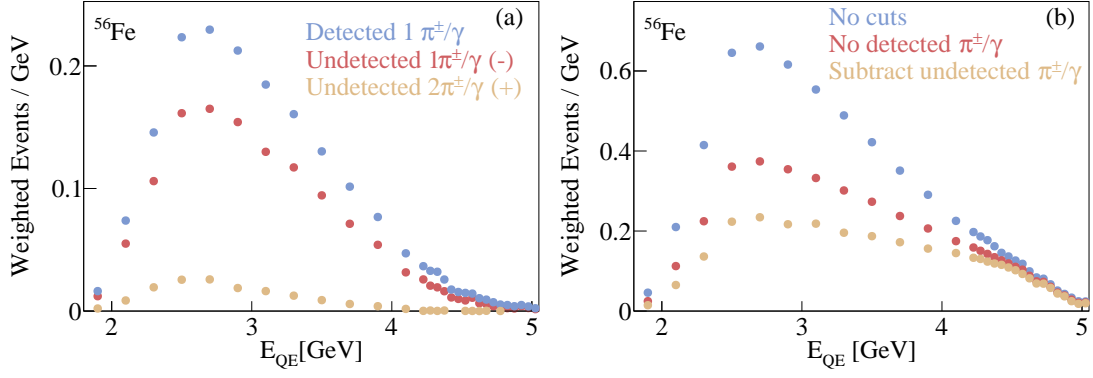
Fig. Extended Data Fig. 7: The effect of undetected pion subtraction. The number of weighted events as a function of reconstructed energy E_{QE} for 4.453 GeV Fe(e, e') events for (Left) events with a detected $\pi^{\pm}$ or photon (blue), events with one (red) or two (light brown) undetected $\pi^{\pm}$ or photons and (Right) all $(e, e'X)$ events with detected or undetected $\pi^{\pm}$ or photon (blue), (e, e') events with no detected $\pi^{\pm}$ or photon (red), and (e, e') events after subtraction for undetected $\pi^{\pm}$ or photon (light brown). The uncertainties are statistical only and are shown at the 1σ or 68% confidence level. Error bars are not shown when they are smaller than the size of the data point.
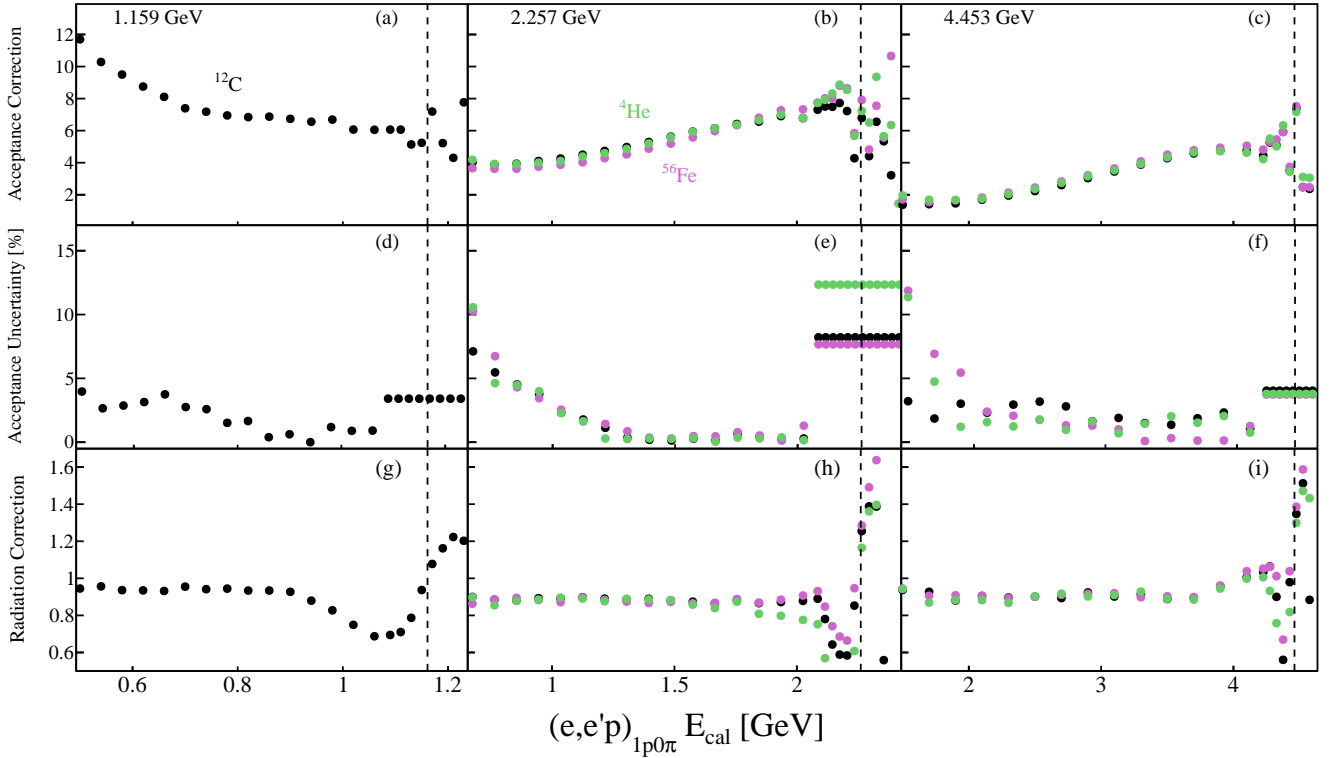

Fig. Extended Data Fig. 8: (top row) Acceptance correction factors, (middle row) acceptance correction factor uncertainties, and (bottom row) electron radiation correction factors plotted vs E_{cal} for the three incident beam energies. Results for carbon are shown in black, helium in green and iron in magenta. The left column (a,d,g) shows the 1.1 GeV results, the middle column (b,e,h) shows the 2.2 GeV results and the right column (c,f,i) shows the 4.4 GeV results.
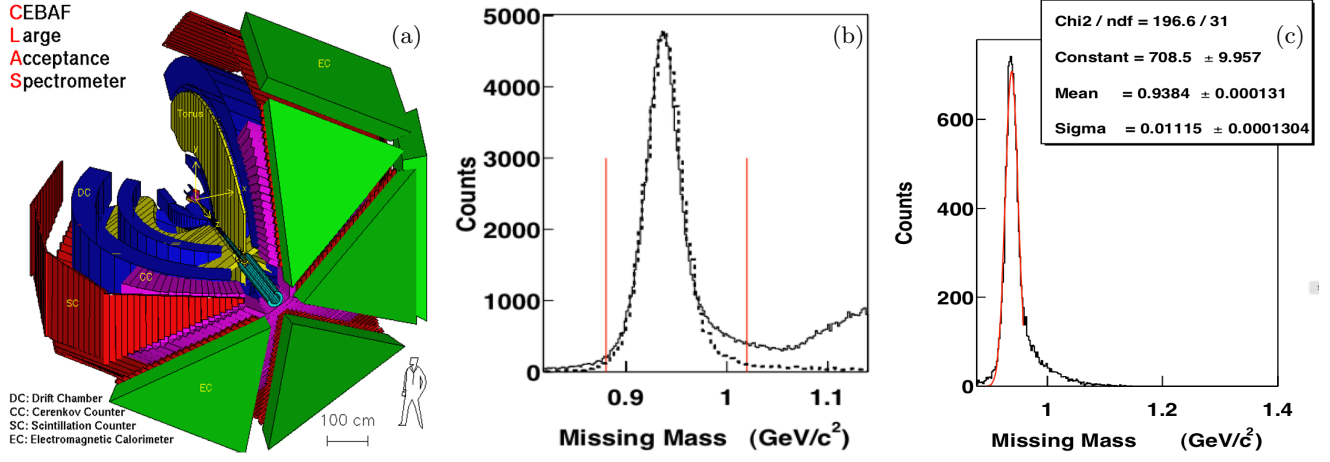
Fig. Extended Data Fig. 9: (left) Cutaway drawing of CLAS showing the sector structure and the different detectors. yellow: toroidal magnet, blue: drift chambers, magenta: cerenkov counter, red: scintillation counters (time of flight), and green: electromagnetic calorimeter. The beam enters from the upper left and the target is in the center of CLAS; (middle) the 2.257 GeV ^{3}He$(e, e'pp)X$ missing mass for (solid histogram) data and (dashed histogram) simulation, and (right) the H$(e, e'\pi^+)X$ missing mass for (black) data and (red) fit to data.